Environmental Science & Technology

pubs.acs.org/est

Article

Reinforcing Covalency via d−p−d Orbital Coupling Enables Dual-Site Selective Ozone Activation for Efficient CH_3SH Mineralization

Rumeng Zhang, Jiahao Huang, Mengliang Hu, Muke Lin, Ji Mei, Shulin Zuo, and Dehua Xia*

Cite This: *Environ. Sci. Technol.* 2025, 59, 26292−26302

Read Online

ACCESS | Metrics & More | Article Recommendations | Supporting Information

ABSTRACT: In catalytic ozonation systems, surface-adsorbed oxygen species ($*O/*O_2$) have emerged as promising non-radical species. They exhibit high reactivity toward electron-rich pollutants and accelerate pre-oxidation via electron-transfer-driven mechanisms. However, their selective generation remains a critical challenge. Herein, we design an amorphous Co−Ni bimetallic oxide ($Co_{0.5}Ni_{0.5}$) with tailored Co(3d)−O(2p)−Ni(3d) orbital coupling, which synergistically enhances metal−oxygen covalency to optimize the bridge adsorption configuration of ozone molecules for efficient activation. The electron-rich Co sites, with optimized 3d e_g orbital occupancy, facilitate π backdonation to ozone, weakening O−O bonds for selective *O formation, while electron-deficient Ni sites stabilize $*O_2$ intermediates via $t_{2g}-\pi^*$ orbital interactions. This dual-site synergy enables 100% CH_3SH mineralization at 600 000 mL h^{-1} g^{-1} with 24 h stability. It also sustains >95% CH_3SH removal over 12 h under 75% relative humidity (attributed to weak H_2O adsorption and enhanced hydrophobicity) while resisting sulfur poisoning through balanced Lewis acidity and high surface −OH density. Through *in situ* spectroscopy and theoretical simulations, we demonstrate that d−p−d orbital hybridization governs both oxygen speciation and interfacial electron transfer kinetics. Our work establishes orbital-level engineering of bimetallic oxides as a universal strategy for sustainable volatile organic compound remediation.

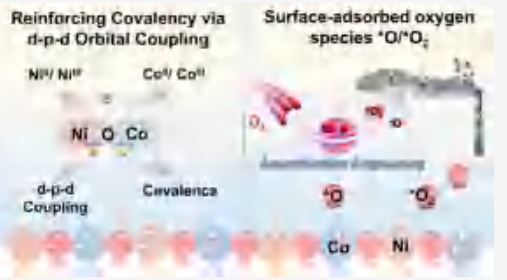

KEYWORDS: *covalency, d−p−d orbital coupling, ozone activation, surface reactive oxygen species ($*O/*O_2$), VOCs*

1. INTRODUCTION

Methyl mercaptan (CH_3SH), a prototypical sulfur-containing volatile organic compound (SVOC) and a key malodor source, has raised intense concern due to its ultralow olfactory threshold (6.7×10^{-5} ppm) and substantial emissions from critical sectors, like petroleum refining and landfill operations. Elevated levels of CH_3SH can result in the formation of secondary aerosols, induce neurotoxicity in humans, cause corrosion of industrial equipment, and lead to catalyst sulfur poisoning and deactivation.[1,2] Heterogeneous catalytic ozonation, an advanced oxidation process (AOP), has emerged as a promising strategy for removing SVOCs owing to its mild conditions and green efficiency.[3,4] Ozone (O_3)-driven degradation proceeds via two distinct pathways: (i) radical routes involving hydroxyl radicals ($^{\bullet}OH$) and superoxide radicals ($^{\bullet}O_2^-$), which exhibit strong but non-selective reactivity, and (ii) non-radical routes mediated by surface-bound oxygen species (e.g., *O and $*O_2$) and singlet oxygen ($^1O_2$).[5] While $^{\bullet}OH$ demonstrates high oxidative potential (E_0 = 2.8 V), its short half-life and indiscriminate reactivity often result in incomplete mineralization, particularly in complex matrices.[6] Recent studies highlight that non-radical oxygen species, particularly *O (2.43 V) and $*O_2$ (1.35 V), generated during ozone decomposition, exhibit exceptional electron-rich VOCs and enhanced stability under realistic conditions.[7] However, the precise activation and control of surface atomic oxygen in conventional catalysts remain insufficient, resulting in poor pathway selectivity and suboptimal degradation of pollutants.

The atomic oxygen pathway confines active sites to the catalyst surface through interfacial effects, effectively eliminating interference from bulk-phase species. This mechanism concurrently enables selective oxidation of surface-adsorbed electron-rich contaminants, endowing the system with both remarkable interference resistance and targeted degradation efficacy for complex sulfurous waste gas treatment. Through electronic structure modulation, the reaction pathway can be directed toward selective oxidation. Specifically, covalent engineering of metal−oxygen bonds (M−O) can precisely optimize the desorption barrier and electrophilicity of *O/$*O_2$, offering a novel approach for designing sulfur-tolerant catalysts and advancing the control of atomic oxygen in catalytic systems.[8−10] Research has shown that asymmetric

Received: August 19, 2025
Revised: November 1, 2025
Accepted: November 3, 2025
Published: November 10, 2025

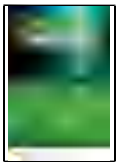

https://doi.org/10.1021/acs.est.5c11499
Environ. Sci. Technol. 2025, 59, 26292−26302

M−O−M configurations in spinel oxides can effectively optimize redox-active sites through covalent interactions.[11] For example, the Ce(4f)−O(2p)−Co(3d) active site precisely regulates the electron density distribution, enhancing electron transfer efficiency and supporting oxidant activation.[12] Similarly, the Bi−O−Co system enables the simultaneous generation of radical and non-radical species through multisite synergy, significantly improving micropollutant removal efficiency.[13] Qu et al. demonstrated that substituting Co sites in Co_3O_4 with Ni cations elevates the d-band center of Co, inducing a bridge-configuration adsorption of ozone at the Co−O−Ni interface and reducing the energy barrier for *O/*O_2 intermediate formation.[8] Fundamentally, cobalt and nickel are strategically selected as the bimetallic pair due to their well-matched ionic radii, moderate electronegativity disparity, and versatile redox couples (Co^{2+}/Co^{3+} and Ni^{2+}/Ni^{3+}), intrinsic attributes that lay a structural and electronic foundation for the synergistic Co−O−Ni interfacial interactions observed in this modulation. These inherent characteristics collectively underscore that enhancing the covalency of Co−Ni bimetallic oxides via d−p−d orbital coupling represents a robust and promising strategy to precisely tune ozone activation pathways, thereby affording a more selective and energy-efficient avenue for catalytic ozonation.

To optimize the generation and stabilization of *O/*O_2 species, precise modulation of the metal−oxygen covalency is essential. Building upon the concept of covalent regulation, amorphous-phase engineering disrupts long-range symmetry, introducing undercoordinated M−O−M sites that facilitate enhanced charge transfer and *O/*O_2 stabilization.[14,15] Unlike crystalline analogues, the dynamic structure of amorphous materials provides flexibility in the electronic configuration, which supports the selective activation of oxygen species. However, most previous studies on amorphous oxide catalysts mainly focused on increasing the density of active sites by utilizing structural disorder but rarely achieved the level of precision at the orbital level in regulating the metal−oxygen covalent bonds to selectively generate active oxygen. Notably, adjusting the surface Lewis acid−base properties (tunable via the amorphous Co−Ni framework) further enhances the interaction between O/O_2 and reactive sites, promoting the targeted adsorption and activation of electron-rich CH_3SH molecules, complementing the structural and orbital-level regulation.[16] This synergy between structural adaptability, orbital-level precision, and acid−base regulation not only ensures superior pollutant degradation but also increases resistance to sulfur poisoning, overcoming the limitations of radical-driven ozonation systems. As a result, this approach presents a promising pathway for designing highly selective, stable, and sulfur-tolerant catalysts for efficient environmental remediation.

Herein, we demonstrate that the amorphization of Co−Ni bimetallic oxides enables precise control over *O/*O_2 generation through asymmetric d−p−d orbital hybridization. This covalent synergy originates from dynamically optimized Co−O−Ni bridge structures, where d−p−d orbital coupling simultaneously enhances metal−oxygen covalency and tailors ozone adsorption geometries. By modulation of the Co/Ni ratio, the dual-site activation and stabilization of *O and *O_2 were achieved. The optimized catalyst achieves complete mineralization at 600 000 mL h^{-1} g^{-1} with 24 h of stability, directly linking its performance to the covalent synergy of the Co−O−Ni framework. This work establishes covalency-driven orbital engineering as a universal paradigm for designing efficient and stable ozone catalysts.

2. MATERIALS AND METHODS

2.1. Synthesis of Co−Ni Bimetallic Oxides with Tunable Crystallinity. A series of Co−Ni bimetallic oxides with Co/Ni molar ratios (x = 0, 0.2, 0.4, 0.5, 0.6, 0.8, and 1) were synthesized via the co-precipitation method. Briefly, 5 mmol of Na_2CO_3 was dissolved in 100 mL of deionized water to form solution A, while $Co(NO_3)_2{\cdot}6H_2O$ and $Ni(NO_3)_2{\cdot}6H_2O$ were dissolved in 100 mL of deionized water to prepare solution B. Both solutions were simultaneously added dropwise into 50 mL of deionized water under stirring with the pH at 9.5. After aging for 1 h, the precipitate was centrifuged (50 mL centrifuge tube: PakGent), washed, and dried at 80 °C for 12 h. The dried precursors were calcined at 350 °C for 3 h (heating rate of 5 °C min^{-1}) to obtain the target catalysts (details of the reagents are shown in Text S1).

2.2. Characterization. The catalysts were characterized by using powder X-ray diffraction (XRD), thermogravimetric analysis (TGA), X-ray photoelectron spectroscopy (XPS), X-ray absorption fine structure spectroscopy (XAFS), Fourier transform infrared spectroscopy (FTIR), temperature-programmed desorption of NH_3/CO_2 (TPD), inductively coupled plasma optical emission spectroscopy (ICP−OES), scanning electron microscopy (SEM), high-angle annular dark-field scanning transmission electron microscopy with energy-dispersive X-ray spectroscopy (HAADF−STEM/EDS), *in situ* diffuse reflectance infrared Fourier transform spectroscopy (*in situ* DRIFTS), *in situ* Raman spectroscopy, electron paramagnetic resonance (EPR), and electrochemical measurements. Detailed experimental parameters are provided in Text S2.

2.3. Catalytic Ozonation Experiments. Catalytic ozonation was performed in a continuous-flow fixed-bed reactor at 25 °C. O_3 was produced by an O_3 generator (YDG, YE-TG-02PII) to a concentration of 50 ppm, with an O_3 flow rate of 12 mL min^{-1}. The stream included humidified synthetic air (RH = 75%) and CH_3SH/N_2 (50 ppm), with a total flow rate of 100 mL min^{-1}. Catalyst beds (10 mg) were loaded into a quartz reactor, and the CH_3SH concentration was monitored in real time using a semiconductor sensor (Detcon DM-400IS). Effluent gases were analyzed by PTR−TOF-MS (H_3O^+ mode, E/N = 120 Td), and exhaust gases were treated via activated carbon adsorption and thermal catalytic oxidation (Pd/Al_2O_3, 300 °C).

The detailed experimental procedures are described in Texts S3−S6.

2.4. Density Functional Theory (DFT) Calculations. Spin-polarized DFT calculations were performed by using VASP 5.4.1 with the PBE functional and a 450 eV cutoff energy. To model the amorphous $Co_{0.5}Ni_{0.5}$ structure, we employed a melt-quench molecular dynamics (MD) approach: (1) A crystalline Co−Ni oxide supercell was melted at 3000 K, followed by rapid quenching to 300 K to simulate amorphization. (2) The resulting structure was optimized until forces converged below 0.02 eV $Å^{-1}$. Adsorption energies were calculated as $E_{ads} = E_{adsorbate/catalyst} - E_{catalyst} + E_{adsorbate}$. Gibbs free energy changes (ΔG) were evaluated using the hydrogen electrode model ($\Delta G = \Delta E_{DFT} + \Delta ZPE - T\Delta S$), and the d-band center (ε_d) was calculated to quantify electronic interactions [$\varepsilon_d = \frac{\int_{-\infty}^{\infty} \varepsilon n_d(\varepsilon) d\varepsilon}{\int_{-\infty}^{\infty} n_d(\varepsilon) d\varepsilon}$]. Detailed computa-

https://doi.org/10.1021/acs.est.5c11499
Environ. Sci. Technol. 2025, 59, 26292−26302

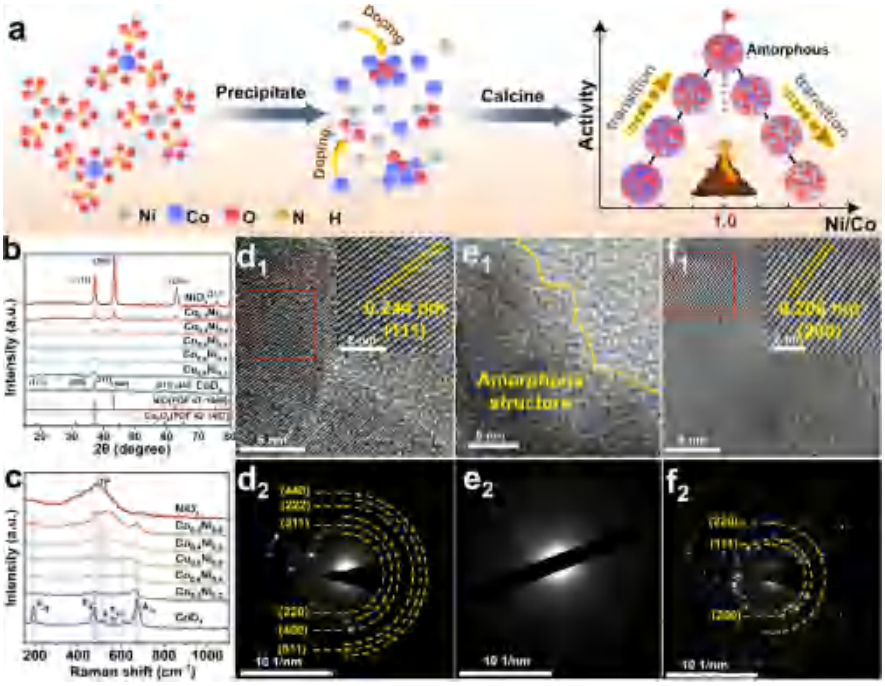

Figure 1. (a) Schematic of solvothermal synthesis and amorphous structure formation of Ni−Co oxides. (b and c) XRD and Raman spectra of the catalysts. HRTEM images and corresponding SAED patterns of (d_1 and d_2) CoO_x, (e_1 and e_2) $Co_{0.5}Ni_{0.5}$, and (f_1 and f_2) NiO_x.

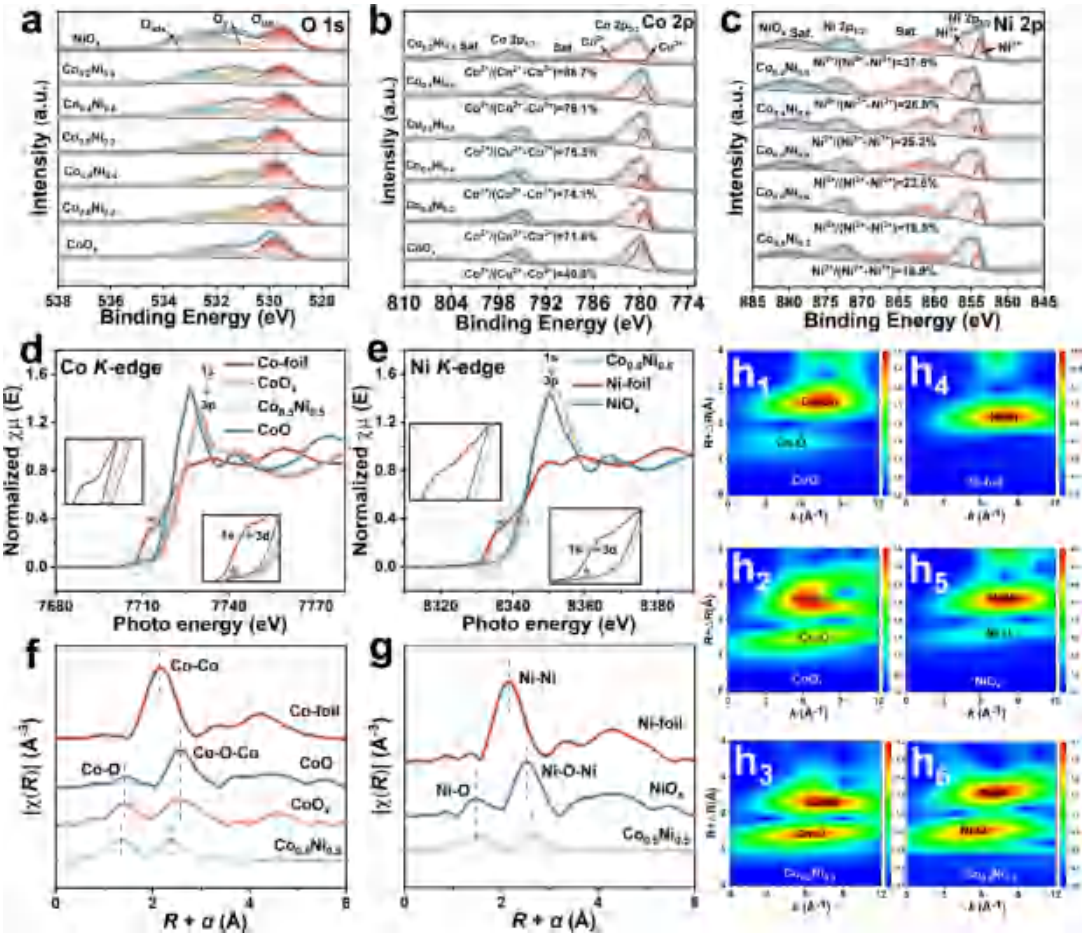

Figure 2. High-resolution XPS spectra: (a) O 1s, (b) Co 2p, and (c) Ni 2p. (d) Normalized Co K-edge XANES spectra. (e) Comparative Ni K-edge XANES spectra. (f and g) Fourier transform (FT) k^2-weighted EXAFS spectra (R space) for Co and Ni coordination environments. (h_{1-6}) Wavelet transform (WT) EXAFS analysis of Co and Ni local structures.

https://doi.org/10.1021/acs.est.5c11499
Environ. Sci. Technol. 2025, 59, 26292−26302

tional methods are provided in Text S7. The amorphous model's validity was confirmed by matching its radial distribution function (RDF) with experimental XAFS data and electronic structure (PDOS) with XPS results.

3. RESULTS AND DISCUSSION

3.1. Structural Evolution and Amorphization-Driven Properties of Ni−Co Bimetallic Oxides. To investigate the structural evolution and amorphous characteristics of the synthesized Ni−Co bimetallic oxides, we systematically characterized their physicochemical properties. A series of Ni−Co oxides with controlled stoichiometries were synthesized via a co-precipitation method (Figure 1a), where precursors with tailored Ni/Co ratios (Figure S1) were calcined to obtain seven distinct compositions (CoO_x to NiO_x). ICP−OES confirms the precise elemental compositions, matching the designed ratios (Table S1).

XRD analysis reveals a structural transition from crystalline to amorphous phases with increasing Co/Ni equivalence (Figure 1b). Monometallic CoO_x and NiO_x show well-defined patterns, which match spinel (PDF 42-1467) and cubic (PDF 47-1049) phases, respectively.[17,18] Bimetallic compositions retain spinel-like structures in Ni-rich samples (Co < 50%) but shift to cubic-like phases in Co-rich systems. Strikingly, the equimolar $Co_{0.5}Ni_{0.5}$ sample shows no Bragg reflections, confirming its amorphous nature. The transition from a crystalline to amorphous structure in $Co_{0.5}Ni_{0.5}$ is further confirmed by Raman spectroscopy (Figure 1c). Amorphous $Co_{0.5}Ni_{0.5}$ displays broadened peaks, indicative of long-range symmetry breaking and localized lattice distortions.[19]

SEM images show that $Co_{0.5}Ni_{0.5}$ possesses a highly porous and interconnected morphology (Figure S2). HRTEM images and selected area electron diffraction (SAED) were employed to further characterize the structural features. As shown in Figure 1$d_{1\ and\ 2}$ and Figure S3, CoO_x exhibits a hexagonal nanoplate morphology, with HRTEM images revealing well-defined lattice fringes of 0.244 nm, corresponding to the (311) plane of spinel Co_3O_4.[20] Similarly, NiO_x shows a lattice spacing of 0.208 nm, consistent with the (200) plane of cubic NiO (Figure 1$f_{1\ and\ 2}$ and Figure S4).[21] The SAED patterns of both CoO_x and NiO_x exhibit sharp diffraction spots, demonstrating their well-ordered crystalline structures, with lattice spacings matching standard crystallographic planes.[22,23] In contrast, the HRTEM images of $Co_{0.5}Ni_{0.5}$ reveal no discernible lattice fringes, and its SAED pattern shows no distinct diffraction spots, unequivocally confirming its amorphous nature (Figure 1$e_{1\ and\ 2}$). Energy-dispersive X-ray spectroscopy (EDS) mapping demonstrates the homogeneous distribution of Ni and Co elements throughout the material (Figure S5).

FTIR (Figure S6a) shows weakened Co−O/Ni−O vibrations (500−750 cm^{-1}), indicating distorted metal−oxygen bonds in disordered Co−O−Ni bridges. The flexible M−O framework exposes undercoordinated metal sites for reactant adsorption, while abundant surface hydroxyls aid sulfur poisoning resistance.[19] NH_3-TPD (Figure S6b) reveals a 609 °C desorption peak, reflecting optimized Lewis acidity from the Co^{3+}/Ni^{2+} synergy in the amorphous structure. This intermediate acid strength effectively adsorbs ozone's electrophilic O terminal via metal−oxygen bonding, avoiding overactivation of irreversible ozone decomposition. CO_2-TPD (Figure S6c) has a 688 °C peak (strongly basic lattice O^{2-}, stabilizing $*O_2$ via electron donation, confirmed by O 1s XPS at 529.2 eV; Figure 2a) and a 273 °C peak (surface hydroxyls).[20] The BET results (Figure S7) do not support the notion that the specific surface area is responsible for the enhanced activity of $Co_{0.5}Ni_{0.5}$.

3.2. Electronic Structure and Coordination Environment. The valence states and local coordination environments of Co and Ni in the catalyst were characterized by XPS (Figure S8) and XAFS. The O 1s spectrum of $Co_{0.5}Ni_{0.5}$ (Figure 2a) can be deconvoluted into lattice oxygen (O_{latt}), vacancy oxygen (O_v), and surface-adsorbed oxygen (O_{ads}). Notably, the oxygen vacancy peak intensity of $Co_{0.5}Ni_{0.5}$ is comparable to crystalline materials, and the EPR results (Figure S9) further corroborate this observation, ruling out oxygen vacancies as the origin of activity differences and supporting our hypothesis that covalent orbital coupling dominates the reaction mechanism. In the Co 2p spectrum (Figure 2b), $Co_{0.5}Ni_{0.5}$ exhibits a higher Co^{2+}/Co^{3+} ratio compared to CoO_x, indicating electron accumulation on Co sites through enhanced Co−O−Ni covalency. Conversely, the Ni 2p spectrum (Figure 2c) shows a lower Ni^{2+} ratio in $Co_{0.5}Ni_{0.5}$ compared to that in NiO_x, demonstrating electron depletion at Ni sites via the O 2p-mediated charge transfer. This charge redistribution creates complementary electronic environments, electron-rich Co and electron-deficient Ni, that are essential for dual-site ozone activation.[24,25]

Normalized Co K-edge XANES spectra (Figure 2d) show that the absorption edge of $Co_{0.5}Ni_{0.5}$ lies between the Co^{2+} and Co^{3+} standards, consistent with XPS results. The pre-edge feature at ∼7710 eV corresponds to the dipole-forbidden 1s to 3d transition, which is sensitive to the symmetry and electron occupancy of Co 3d orbitals. Crystal field splitting separates the Co 3d orbitals into lower energy t_{2g} (d_{xy}, d_{xz}, and d_{yz}) and higher energy e_g ($d_{x^2-y^2}$ and d_{z^2}) states. The partial e_g orbital occupancy, modulated by the disordered Co−O−Ni framework, facilitates π back donation to ozone's antibonding orbitals, thereby promoting selective O−O bond cleavage. The Ni K-edge (Figure 2e) displays a 0.6 eV blue shift in $Co_{0.5}Ni_{0.5}$ compared to Ni^{2+}, confirming the prevalence of Ni^{3+} species that create electron-deficient sites for stabilizing oxygen intermediates.[26]

EXAFS spectra (Figure 2f and g) reveal the first coordination shells around Co and Ni. In $Co_{0.5}Ni_{0.5}$, the Co−O bond length (1.5 Å) is shorter than that in crystalline CoO_x (1.62 Å), while the Ni−O bond length (1.6 Å) is reduced compared to that in NiO_x (1.68 Å), demonstrating strengthened M−O covalency through d−p−d orbital hybridization. These shortened bonds correlate with enhanced electron density overlap, which is crucial for efficient charge transfer during ozone activation. Wavelet transform (WT) analysis (Figure 2h_{1-6} and Figure S10) further confirms the structural disorder in $Co_{0.5}Ni_{0.5}$. Unlike crystalline counterparts that show sharp intensity maxima at specific (k, R) coordinates, the amorphous sample exhibits diffuse WT features, characteristic of short-range ordered Co−O−Ni bridges with configurational heterogeneity. The Co K-edge EXAFS oscillation function (Figure S11a) for $Co_{0.5}Ni_{0.5}$ shows distinct phase shifts compared to CoO and Co_2O_3, reflecting altered scattering pathways from amorphous Co−O−Ni bridges. Similarly, the Ni K-edge oscillation (Figure S11b) deviates from NiO, verifying modified coordination environments.[27,28]

3.3. Covalency-Driven Electronic Structure and d−p−d Orbital Hybridization. DFT calculations reveal the electronic structure and orbital interactions in the Co−Ni bimetallic oxides. Figure S12 shows the optimized theoretical

https://doi.org/10.1021/acs.est.5c11499
Environ. Sci. Technol. 2025, 59, 26292−26302

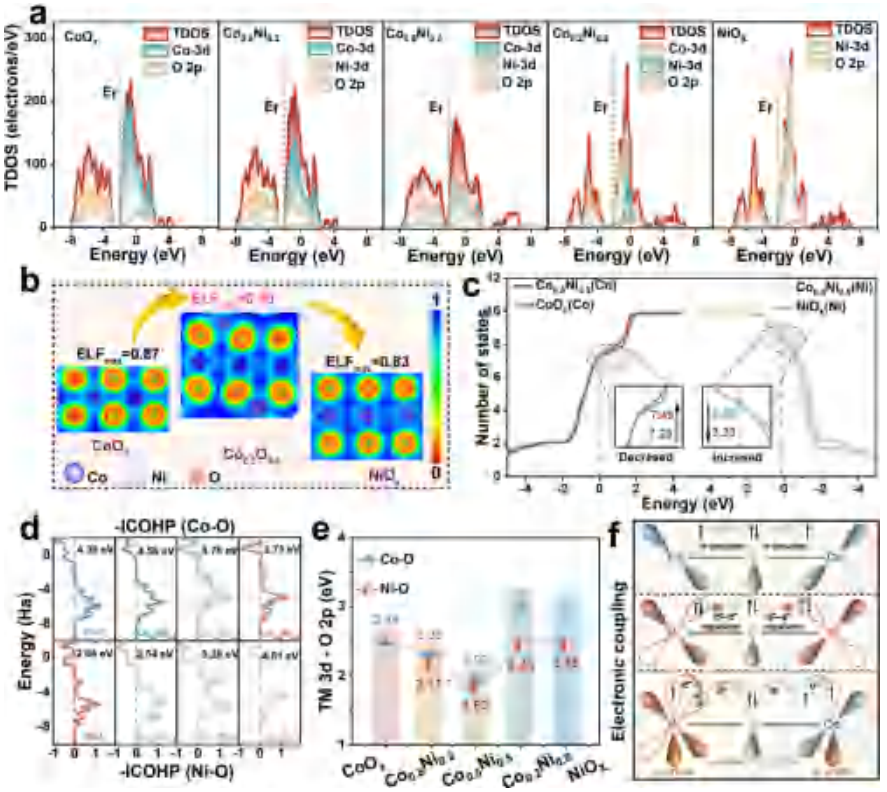

Figure 3. (a) PDOS near the Fermi level of catalysts. (b) ELF cross sections with isosurface values. (c) 3d electron counts of Co/Ni sites. (d) COHP of metal−oxygen bonds. (e) Covalency of Co−O/Ni−O bonds. (f) Proposed electronic coupling via 3d orbital hybridization.

model. The PDOS near the Fermi level (E_f) (Figure 3a) reveals critical distinctions in the electronic behavior across catalysts. Crystalline CoO_x and NiO_x exhibit distinct band gaps between the O 2p valence band and Co/Ni 3d conduction band, indicating limited electron mobility and weak M−O covalency.[29] In contrast, the amorphous $Co_{0.5}Ni_{0.5}$ catalyst displays a zero band gap at E_f, with Co 3d and Ni 3d states merging seamlessly with the O 2p states across a broad energy range. This demonstrates robust Co(3d)−O(2p)−Ni(3d) orbital hybridization, where delocalized electron density forms a continuous energy band conducive to rapid charge transfer. In EXAFS, the K-edge shifts of Co and Ni confirm the electron enrichment at Co and depletion of Ni sites in the amorphous structure, consistent with PDOS-derived orbital occupancy conclusions. Electron localization function (ELF) analysis (Figure 3b) shows enhanced delocalization in the amorphous Co−O−Ni framework with maximum ELF values (0.90) exceeding those of crystalline CoO_x (0.87) and NiO_x (0.83). This reflects strong covalent bonding from asymmetric d−p−d hybridization, where Co(3d)−O(2p)−Ni(3d) orbital overlap adapts dynamically to intermediate adsorption geometries. As shown in Figure 3c, electron counting was performed to quantify 3d orbital occupancy, revealing 7.49 electrons in the Co 3d orbitals and 8.23 electrons in the Ni 3d orbitals. These results validate the electron redistribution hypothesis, explaining the facilitated electron transfer from Ni to Co via O^{2-} bridges that enhances ozone decomposition activity.[15,30]

Crystal orbital Hamilton population (COHP) analysis (Figure 3d) quantifies the M−O bond strength, revealing higher −ICOHP values for Co−O (4.76 eV) and Ni−O (5.28 eV) in $Co_{0.5}Ni_{0.5}$ compared to their crystalline counterparts. The higher −ICOHP values indicate stronger covalent bonding, promoting ozone dissociation via enhanced charge transfer while preserving optimal intermediate adsorption strength, crucial for selective non-radical pathways. Comparative covalency analysis (Figure 3e) confirms stronger Co−O−Ni covalency due to synergistic 3d−2p−3d hybridization. Figure 3f depicts the proposed coupling mechanism in the Co−Ni bimetallic oxide: 3d orbital hybridization drives electron transfer from Co to Ni antibonding orbitals via O 2p bridges, yielding a hybridized Co(3d)−O(2p)−Ni(3d) network. This enhanced covalency fosters an electronic environment favorable for subsequent ozone interaction. We propose that this optimized electronic configuration aligns well with ozone's molecular orbitals, facilitating ozone activation via O−O bond weakening through π back donation and orbital interactions upon adsorption.

3.4. Catalytic Performance and Non-radical Pathway Mechanism. The catalytic ozonation performance of bimetallic Co−Ni oxides was systematically evaluated for CH_3SH degradation (Figure S13 illustrates a schematic diagram of the catalytic ozonation reaction setup). Figures S14 and S15 present the calculated molecular orbital energy levels and electrostatic potential maps of the corresponding atomic groups of the ions of O_3 and CH_3SH, respectively, providing insights into their electronic and chemical properties. The amorphous $Co_{0.5}Ni_{0.5}$ catalyst achieved complete CH_3SH mineralization under a continuous ozone flow (Figure 4a), outperforming monometallic oxides and other bimetallic compositions. A volcano-shaped correlation was observed between the mass-normalized activity and the Ni/Co molar ratio, with the $Co_{0.5}Ni_{0.5}$ composition located at the apex (Figure 4b and Figure S16). This correlation coincided with

https://doi.org/10.1021/acs.est.5c11499
Environ. Sci. Technol. 2025, 59, 26292−26302

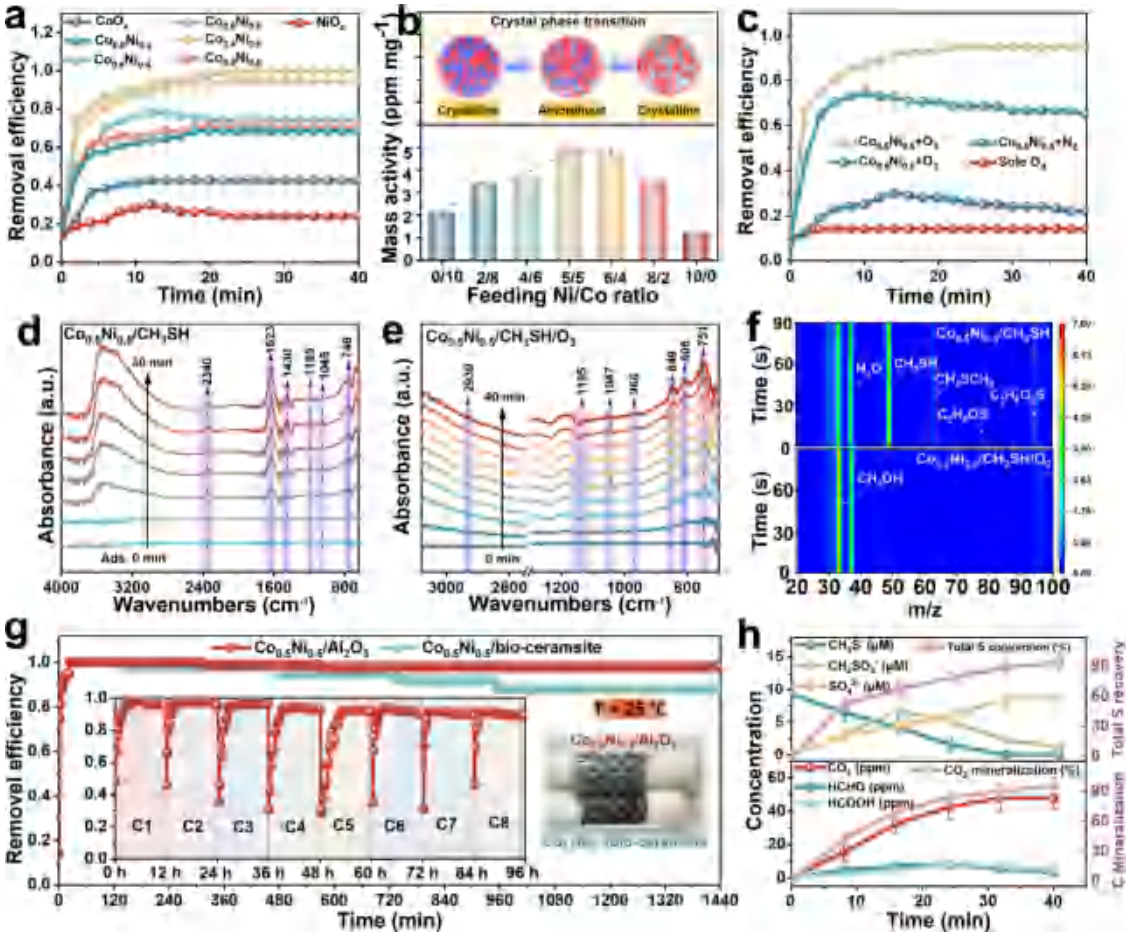

Figure 4. (a) CH_3SH removal efficiency over time. (b) Mass activity over the crystalline-phase transition. (c) Removal efficiency under varied gas compositions. (d and e) *In situ* DRIFT of $Co_{0.5}Ni_{0.5}$ during CH_3SH adsorption and catalytic ozonation of CH_3SH. (f) PTR−TOF-MS of CH_3SH degradation products. (g) Long-term stability (CH_3SH/O_3 flow; inset: 8 regeneration cycles). (h) Time-dependent concentrations of sulfur/carbon species in the $Co_{0.5}Ni_{0.5}/O_3$ system.

the structural transition from the crystalline to amorphous phases.

Control experiments elucidate the ozone-specific activation mechanism by $Co_{0.5}Ni_{0.5}$ (Figure 4c). The catalytic system achieved limited CH_3SH removal efficiency (<20%) when employing ozone alone. Remarkably, synergistic effects emerged when the $Co_{0.5}Ni_{0.5}$ catalyst was combined with ozone, enabling complete contaminant degradation (100% removal) within the experimental duration. Comparative studies showed intermediate efficiency (60%) in the O_2-assisted system, while N_2 co-feeding yielded minimal improvement (24% removal). These results demonstrate the critical dependence of reactive oxygen species generation on catalytic ozone activation, with the $Co_{0.5}Ni_{0.5}$ catalyst exhibiting superior performance in facilitating ozone-derived reactive oxygen species formation compared to molecular oxygen activation pathways. As summarized in Table S2, the $Co_{0.5}Ni_{0.5}/O_3$ system exhibits a mass activity of 5.00 ppm of mg^{-1}, surpassing well-documented Ag/MnO_2 and spinel oxides, demonstrating its exceptional efficiency.

In situ DRIFT elucidates the CH_3SH degradation process over the amorphous $Co_{0.5}Ni_{0.5}/O_3$ system. During CH_3SH adsorption, characteristic vibrations at 1045 cm^{-1} (C−S stretching) and 1430 cm^{-1} (CH_3 bending) confirm chemisorption via coordination of sulfur to surface metal sites (Figure 4d). Upon ozone introduction, new peaks emerge at 751 cm^{-1} (C−H stretching in partially oxidized intermediates), 806 cm^{-1} (S−O stretching in sulfonate species), and 968 cm^{-1} (symmetric SO_4^{2-} stretching), accompanied by the gradual disappearance of C−S and CH_3 signals (Figure 4e). Concurrently, carboxylate intermediates (COO^-, 849 and 1185 cm^{-1}) and gaseous CO_2 (2340 cm^{-1}) are detected, confirming complete carbon backbone fragmentation and mineralization (Figure S17).

Gas-phase organic compounds (Figure 4f and Table S3) were comprehensively characterized using PTR−TOF-MS. In the absence of ozone, incomplete CH_3SH degradation yielded three predominant sulfur-containing byproducts: dimethyl sulfide (CH_3SCH_3, m/z 63), dimethyl sulfoxide (C_2H_6OS, m/z 79), and dimethyl sulfone ($C_2H_6O_2S$, m/z 95). Notably, the catalytic ozonation system eliminated both CH_3SH and its derivatives from effluent gases, demonstrating effective mineralization through advanced oxidation processes. The transient detection of methanol (CH_3OH, m/z 33) confirms its role as a reaction intermediate during the oxidative degradation pathway.

For improved practicality and reaction efficiency, the $Co_{0.5}Ni_{0.5}$ catalyst was immobilized on bioceramsite and activated Al_2O_3 (Figure 4g inset), enabling scalable use while retaining excellent long-term stability under continuous flow. Notably, porous, highly dispersed $Co_{0.5}Ni_{0.5}/Al_2O_3$ maintained 98% efficiency after 24 h of continuous operation and >85%

https://doi.org/10.1021/acs.est.5c11499
Environ. Sci. Technol. 2025, 59, 26292−26302

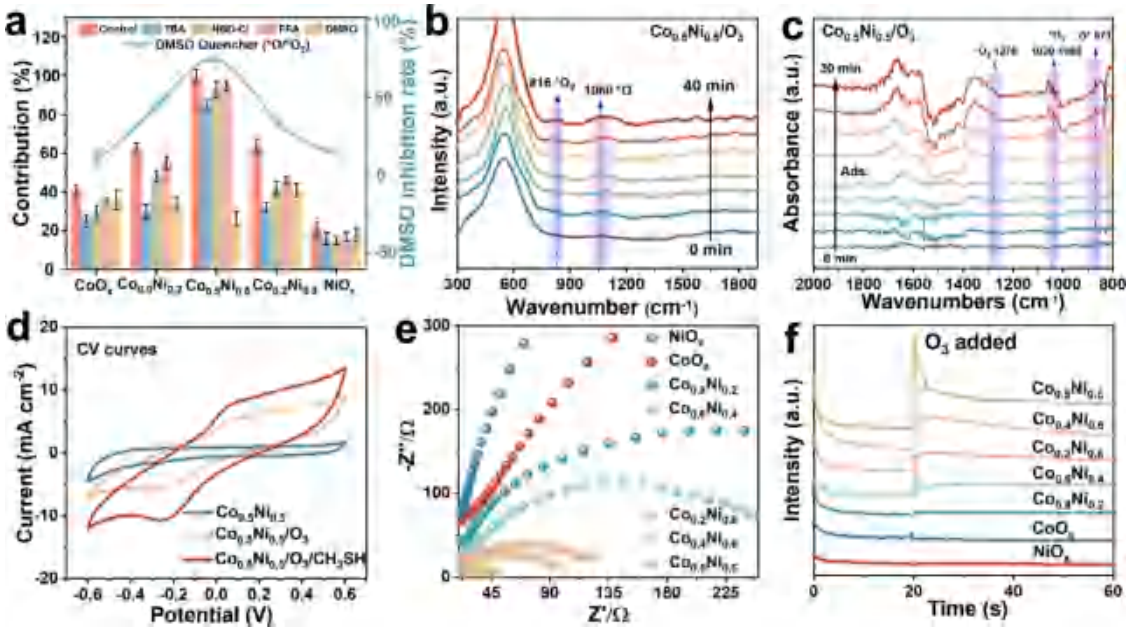

Figure 5. (a) Reactive species contribution (different systems). (b and c) *In situ* Raman spectra and DRIFT. (d) $C-v$ curves of the $Co_{0.5}Ni_{0.5}$ system. (e) Electrochemical impedance spectroscopy (EIS) Nyquist plots. (f) Current−time ($i-t$) responses.

degradation rate after 8 cycles. Under high humidity (75% RH), the supported catalyst still achieved >95% CH_3SH removal over 12 h (Figure S18). The contact angle increases with optimized electron complementarity (bimetallic interactions lowering surface polarity) and amorphous-induced microroughness, enhancing hydrophobicity (Figure S19). As calculated (Figure S20), H_2O adsorption energies on $Co_{0.5}Ni_{0.5}$ are only −0.45 eV (Co sites) and −0.30 eV (Ni sites), weak interactions that explain humidity's minimal impact on CH_3SH removal. Moreover, post-reaction analysis confirmed structural stability: slight surface area reduction (Figure S21), minor valence adjustments (Figure S22), and retained amorphous characteristics (Figures S23−S25).

Ion chromatography (IC) was used to monitor the product evolution of CH_3SH mineralization over $Co_{0.5}Ni_{0.5}$. As shown in Figure 4h and Tables S4 and S5, key sulfur intermediates (CH_3S^-, $CH_3SO_3^-$, and SO_4^{2-}) evolved dynamically, and high total sulfur recovery confirmed complete sulfur balance. For carbon species, CO_2 rose continuously alongside HCHO/HCOOH intermediates, with efficient carbon conversion to CO_2 validating a robust carbon balance. These results demonstrate that the catalyst drives CH_3SH oxidation to less toxic CO_2 and SO_4^{2-}.

Notably, the excellent sulfur poisoning resistance of the $Co_{0.5}Ni_{0.5}$ catalyst is attributed to strong Co−O−Ni interactions from d−p−d orbital hybridization-tailored surface acid−base behavior, with balanced Lewis acidity (Figure S6b) precluding excessive SO_2 adsorption or inefficient activation. Meanwhile, CO_2-TPD (Figure S6c) and FTIR (Figure S6a, 3430/1380 cm^{-1}) confirm its highest surface −OH density, which weakens S−O bonding to suppress sulfate deposition.

ESR spectra further characterized ROS in different systems during 20 min of ozone activation (Figure S26a): the $Co_{0.5}Ni_{0.5}/O_3$ system showed no significant radicals (DMPO−$^{\bullet}$OH and DMPO−$^{\bullet}O_2^-$), while distinct $^{\bullet}$OH and $^{\bullet}O_2^-$ signals were detected in $Co_{0.2}Ni_{0.8}$ and $Co_{0.8}Ni_{0.2}$ systems. This indicates that ozone activation by amorphous $Co_{0.5}Ni_{0.5}$ does not proceed via traditional radical pathways. TEMP−$^1O_2$ signals were detected in all systems, but $Co_{0.5}Ni_{0.5}$ exhibited signal intensity comparable to NiO_x (with negligible catalytic ozonation performance) and lower than CoO_x, $Co_{0.8}Ni_{0.2}$, and $Co_{0.2}Ni_{0.8}$ systems, suggesting that $^1O_2$ is not the primary active species for pollutant mineralization. Given the growing focus on surface-reactive species, these results strongly imply that surface-bound $*O/*O_2$ species dominate the mineralization process.

3.5. Reactive Species Identification and Electron Transfer Kinetics. The contribution of reactive oxygen substances was systematically probed by using radical scavengers (Figure 5a). In the $Co_{0.5}Ni_{0.5}/O_3$ system, the addition of DMSO (a $*O/*O_2$ quencher) drastically reduced CH_3SH removal efficiency from 100 to 23%, whereas *tert*-butanol (TBA, $^{\bullet}$OH scavenger), NBD−Cl ($^{\bullet}O_2^-$ scavenger), and furfuryl alcohol (FFA, $^1O_2$ scavenger) had negligible effects. This confirms that surface-adsorbed $*O/*O_2$ species are the primary oxidants, aligning with the ESR spectra. The green curve demonstrates that the contribution rate of $*O/*O_2$ exhibits a volcano-type trend with changes in the catalyst composition ratio, with the amorphous $Co_{0.5}Ni_{0.5}$ system positioned at the apex of the volcano. In contrast, crystalline $Co_{0.2}Ni_{0.8}$ and $Co_{0.8}Ni_{0.2}$ exhibited significant radical-dependent pathways, underscoring the amorphous catalyst's unique ability to steer ozone activation toward non-radical routes via covalent orbital coupling.

In situ Raman and DRIFT spectra (Figure 5b and c) monitor the ozone adsorption and intermediate evolution. Upon O_3 introduction, characteristic peaks at 1060 cm^{-1} assigned to surface-adsorbed atomic oxygen *O and 816 cm^{-1} assigned to $*O_2$ appear on $Co_{0.5}Ni_{0.5}$ within 10 min in Raman spectra.[19,25,31] The peaks at 871 and 1276 cm^{-1} in the DRIFT spectra further confirm this phenomenon, serving as direct evidence for the non-radical surface reactive species $*O/*O_2$ in the amorphous $Co_{0.5}Ni_{0.5}/O_3$ system. This validates our hypothesis that modulating the covalency through an amorphous strategy enables a shift in the ozone catalytic pathway.

https://doi.org/10.1021/acs.est.5c11499
Environ. Sci. Technol. 2025, 59, 26292−26302

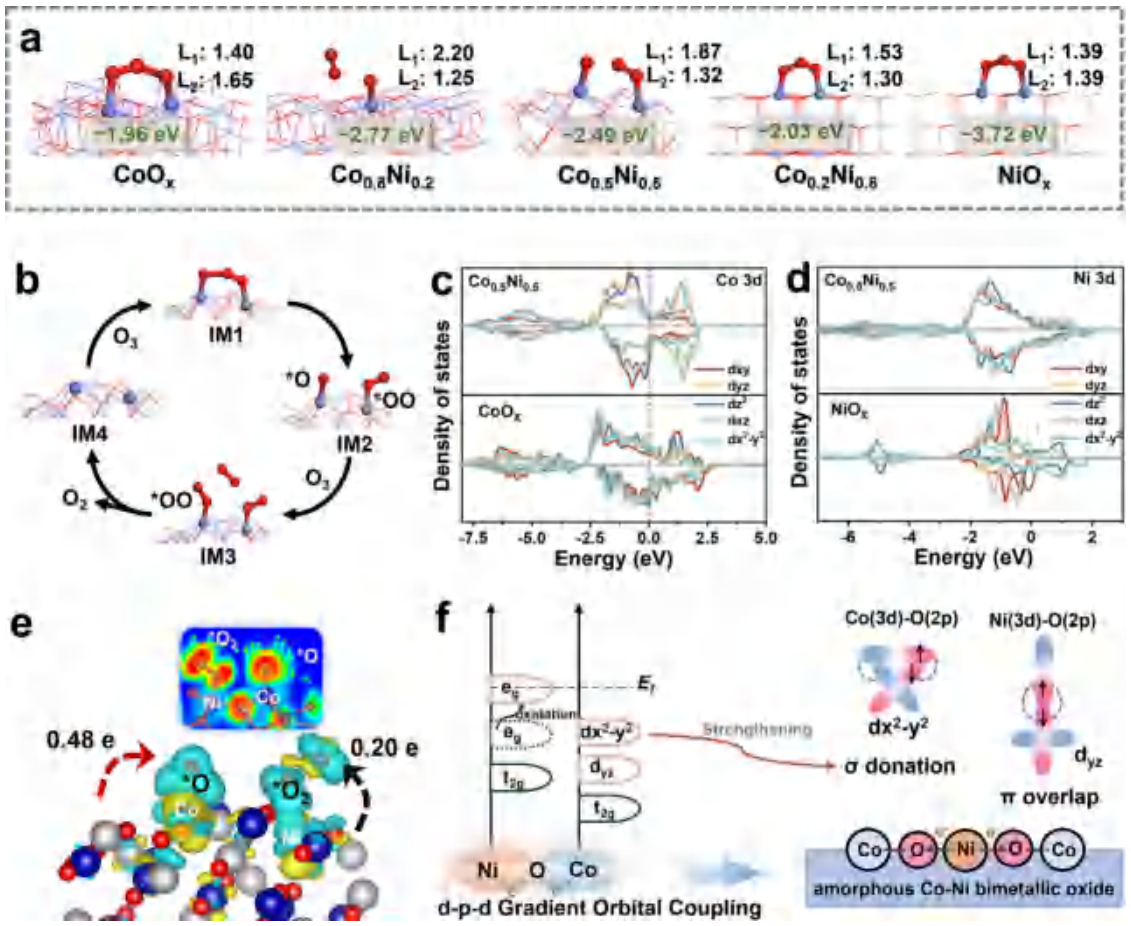

Figure 6. (a) Optimized adsorption configurations of ozone molecules. (b) O_3 activation process on the $Co_{0.5}Ni_{0.5}$ catalyst. PDOS of (c) Co 3d and (d) Ni 3d. (e) ELF, differential charge density, and interfacial charge transfer. (f) Schematic of electronic modulation and orbital coupling.

The cyclic voltammetry (CV) curve (Figure 5d) shows that the addition of O_3 and CH_3SH in the $Co_{0.5}Ni_{0.5}/O_3$ system enhances the redox peak signal, indicating stronger surface reactions and electron transfer. The Nyquist plots (Figure 5e) reveal that the semicircle radius for $Co_{0.5}Ni_{0.5}$ is remarkably smaller than those of crystalline metal oxides, directly reflecting a substantially lower charge transfer resistance. This phenomenon arises from the amorphous structure's enhanced covalent Co(3d)−O(2p)−Ni(3d) orbital coupling, which creates a delocalized electron network that accelerates interfacial charge transport. The zero band gap eliminates energy barriers for electron transfer, enabling rapid ozone activation via efficient π back donation from hybridized orbitals to the π^* orbitals of O_3. These results directly validate that covalency-driven electronic structure optimization is the mechanistic origin of the catalyst's superior charge transfer kinetics and non-radical reactivity. As theoretically speculated, the $i-t$ curves (Figure 5f and Figure S28) further demonstrate the superior stability of $Co_{0.5}Ni_{0.5}$, maintaining a stable current density over ozone exposure. In contrast, other mono- and bimetallic crystalline oxides exhibit a rapid current decay, highlighting their limited durability under reaction conditions.

3.6. Ozone Adsorption Configuration and Orbital Interaction Mechanism. DFT calculations (Figure 6a) reveal distinct adsorption behaviors of O_3 across catalysts. On CoO_x, O_3 adsorbs weakly (−1.96 eV) with minimal structural distortion; bond lengths (L_1, O1−O2; L_2, O2−O3) remain nearly identical to gaseous O_3, leading to insufficient O−O bond activation. By contrast, NiO_x exhibits excessively strong O_3 adsorption (−3.72 eV), overstabilizing O_3 to thermodynamically hinder dissociation. Both extremes (weak/strong adsorption) impair oxidative activation: the former blocks bond cleavage, while the latter deactivates catalytic sites, consistent with experimental observations.

Notably, mixed oxides ($Co_{0.8}Ni_{0.2}$ and $Co_{0.2}Ni_{0.8}$) induce significant O_3 distortion upon adsorption, driving direct cleavage into mobile $^{\bullet}O_2$ free oxygen species. ESR spectroscopy confirms the subsequent conversion of $^{\bullet}O_2$ to reactive oxygen species ($^1O_2$, $^{\bullet}O_2^-$, and $^{\bullet}OH$). Strikingly, $Co_{0.5}Ni_{0.5}$ achieves optimal O_3 activation: adsorbed O_3 dissociates into stable *O (anchored on Co) and $*O_2$ (on Ni) (Figure 6b). By combining the quenching experiments with XPS analysis, we found a significant quantitative correlation between the degree of balance of Co^{2+}/Ni^{3+} sites and the generation efficiency of $*O/*O_2$ (Figure S26b−d). When the value of $|Co^{2+}\% - Ni^{3+}\%|$ is the smallest, the amorphous $Co_{0.5}Ni_{0.5}$ catalyst exhibits the highest $*O/*O_2$ contribution rate. This result quantitatively confirms the core role of electron-rich Co^{2+} and electron-deficient Ni^{3+} in the dual-site cooperative activation of O_3, which is highly consistent with the theoretical predictions of DFT.[32] To clarify the CH_3SH/O_3 interplay, DFT (Figure S29) shows that CH_3SH adsorbs more weakly on $Co_{0.5}Ni_{0.5}$ (−1.55 eV on Co and −0.63 eV on Ni) than on O_3 (−2.49 eV). Thiol introduction also enables atomic oxygen to locally degrade adjacent adsorbed thiols, particularly accelerating cleavage of the C−S bond. The process of ozonation of

https://doi.org/10.1021/acs.est.5c11499
Environ. Sci. Technol. 2025, 59, 26292−26302

CH_3SH on the surface of the $Co_{0.5}Ni_{0.5}$ catalyst surface mainly includes four stages (eqs 1−4): (1) adsorption and thiolate formation ($\equiv M-SCH_3$), (2) sulfur coupling and carbon hydroxylation, (3) deep oxidation, and (4) final mineralization.

$$\equiv M-SCH_3 + {}^*O_2/{}^*O \rightarrow CH_3SSCH_3 + \equiv M-OCH_3 \quad (1)$$

$$\equiv M-OCH_3 + H_2O \rightarrow CH_3OH + {}^*O \rightarrow HCHO + {}^*O \rightarrow CO_2 + H_2O \quad (2)$$

$$CH_3SSCH_3 + {}^*O_2 \rightarrow 2CH_3SO \quad (3)$$

$$CH_3SO + {}^*O \rightarrow CH_3SO_3^- + {}^*CH_3SO_3^- + {}^*O_2 \rightarrow SO_4^{2-} + CO_2 + H_2O \quad (4)$$

TDOS results show that d−p−d orbital coupling in amorphous $Co_{0.5}Ni_{0.5}$ controls the selective dissociation of O_3 into surface-adsorbed *O and $*O_2$. PDOS analyses (Figure 6c and d) demonstrate that Ni integration fundamentally restructures the electronic landscape: Co 3d orbitals exhibit e_g band broadening and an upshift in the d-band center relative to CoO_x. This configuration enhances π back donation into the O_3 π antibonding orbitals, weakening the O−O bonds. Conversely, Ni sites display depleted t_{2g} states below E_F and emergent π orbitals above E_F, serving as electron-deficient reservoirs for $*O_2$ stabilization.[33,34] The provided 2D ELF (Figure 6e) plot shows charge distribution after *O and $*O_2$ adsorption on Co and Ni sites. Higher ELF values between Co and *O indicate strong covalent bonding with significant electron sharing, enabling effective π back donation to weaken the O−O bonds. A diffuse ELF distribution near $*O_2$ reflects the electron-deficient nature, facilitating charge acceptance from the σ orbital of $*O_2$.[35,36]

Figure 6f shows the d−p−d gradient orbital coupling in amorphous Co−Ni bimetallic oxide: Co−O−Ni structures gain stronger covalency via overlapping Co(3d)−O(2p) and Ni(3d)−O(2p) orbitals, leading to changes in the 3d orbitals of Co and Ni. Co 3d e_g orbitals show an increase in electron occupancy, while Ni 3d orbitals contribute to the overall electron distribution within the structure. With O_3 introduction, electron-rich Co sites (with altered 3d orbitals) donate σ electrons to O_3, while Ni sites engage in π overlap. This orbital interplay adjusts O_3 to a double-tooth adsorption geometry, promoting selective formation of surface-bound non-radical species, key for efficient catalysis.

4. ENVIRONMENTAL IMPLICATION

Volatile organic compounds (VOCs) are pervasive environmental hazards that contribute to air pollution, ozone formation, and human health risks. Conventional catalytic ozonation suffers from poor mineralization and radical-induced byproducts, restricting its practical use. This work addresses these issues by developing an amorphous Co−Ni bimetallic oxide catalyst, which leverages d−p−d orbital coupling for dual-site selective O_3 activation. The $Co_{0.5}Ni_{0.5}$ oxide features flexible Co(3d)−O(2p)−Ni(3d) hybridization (enhancing Co−O−Ni covalency) and achieves complete CH_3SH mineralization at an industrial-grade space velocity of 600 000 mL h^{-1} g^{-1}, outperforming advanced existing systems.

Notably, the non-radical pathway (mediated by surface *O/$*O_2$) eliminates toxic sulfur byproducts (e.g., dimethyl sulfoxide/sulfone), reducing secondary pollution. Excellent moisture resistance and sulfur poisoning resistance ensure its reliability in industrial waste gas treatment. Additionally, cost analysis (Table S6) confirms that using earth-abundant Co/Ni aligns with green chemistry, offering a cost-effective, sustainable solution. This orbital-engineering strategy provides a blueprint for next-generation catalysts to meet the sustainable development goal (SDG) targets of air quality improvement and sustainable industrialization.

■ ASSOCIATED CONTENT

Supporting Information

The Supporting Information is available free of charge at https://pubs.acs.org/doi/10.1021/acs.est.5c11499.

Details of experimental procedures, characterization details of samples, including SEM, TEM, BET, CO_2/NH_3-TPD, TG, XPS, EPR, and EXAFS, ESR spectra of different samples for $^1O_2$, $^\bullet O_2^-$, and $^\bullet OH$, *in situ* DRIFTS spectra, chronoamperometric (i−t) curves, DFT calculations and more catalytic data, and performance and cost comparison tables (PDF)

■ AUTHOR INFORMATION

Corresponding Author

Dehua Xia − *School of Environmental Science and Engineering, Sun Yat-sen University, Guangzhou 510275, China; Guangdong Key Laboratory of Environmental Pollution, Guangzhou 510275, China;* orcid.org/0000-0001-6016-358X; Email: xiadehua3@mail.sysu.edu.cn

Authors

Rumeng Zhang − *School of Environmental Science and Engineering, Sun Yat-sen University, Guangzhou 510275, China*

Jiahao Huang − *School of Environmental Science and Engineering, Sun Yat-sen University, Guangzhou 510275, China*

Mengliang Hu − *School of Materials, Sun Yat-Sen University, Shenzhen 518107, China;* orcid.org/0009-0005-5564-5943

Muke Lin − *School of Environmental Science and Engineering, Sun Yat-sen University, Guangzhou 510275, China*

Ji Mei − *School of Environmental Science and Engineering, Sun Yat-sen University, Guangzhou 510275, China*

Shulin Zuo − *School of Environmental Science and Engineering, Sun Yat-sen University, Guangzhou 510275, China*

Complete contact information is available at: https://pubs.acs.org/10.1021/acs.est.5c11499

Notes

The authors declare no competing financial interest.

■ ACKNOWLEDGMENTS

The authors acknowledge financial support from the National Natural Science Foundation of China (41603097, 21673086, 52070195, 32071322, and 22476221) and the Guangdong Basic and Applied Basic Research Foundation (2022B1515020097). The authors also would like to thank Shiyanjia Lab (www.shiyanjia.com) and SCI-GO (www.sci-go.com) for providing EPR and XPS tests, respectively.

REFERENCES

(1) Qu, W.; Tang, Z.; Tang, S.; Zhong, T.; Zhao, H.; Tian, S.; Shu, D.; He, C. Precisely constructing orbital coupling-modulated iron dinuclear site for enhanced catalytic ozonation performance. *Proc. Natl. Acad. Sci. U.S.A.* **2024**, *121* (16), No. e2319119121.

(2) Huang, H.; Xie, X.; Xiao, F.; Liu, B.; Zhang, T.; Feng, F.; Lan, B.; Zhang, C. A Critical Review of Deep Oxidation of Gaseous Volatile Organic Compounds via Aqueous Advanced Oxidation Processes. *Environ. Sci. Technol.* **2024**, *58* (42), 18456−18473.

(3) Ma, D.; Lian, Q.; Zhang, Y.; Huang, Y.; Guan, X.; Liang, Q.; He, C.; Xia, D.; Liu, S.; Yu, J. Catalytic ozonation mechanism over $M_1-N_3C_1$ active sites. *Nat. Commun.* **2023**, *14* (1), 7011.

(4) Chen, W.; He, H.; Liang, J.; Wei, X.; Li, X.; Wang, J.; Li, L. A comprehensive review on metal based active sites and their interaction with O_3 during heterogeneous catalytic ozonation process: Types, regulation and authentication. *J. Hazard. Mater.* **2023**, *443*, 130302.

(5) Yu, G.; Wang, J.; Xu, Z.; Cao, H.; Dai, Q.; Wu, Y.; Xie, Y. Synergetic Manipulation Mechanism of Single-Atom $M-N_4$ and M−OH (M = Mn, Fe, Co, Ni) Sites for Ozone Activation: Theoretical Prediction and Experimental Verification. *Environ. Sci. Technol.* **2024**, *58* (21), 9393−9403.

(6) Ren, T.; Yin, M.; Chen, S.; Ouyang, C.; Huang, X.; Zhang, X. Single-Atom Fe-N_4 Sites for Catalytic Ozonation to Selectively Induce a Nonradical Pathway toward Wastewater Purification. *Environ. Sci. Technol.* **2023**, *57* (9), 3623−3633.

(7) Zhang, R.; Zhou, H.; Shao, T.; Lian, Q.; Hu, M.; Mei, J.; Zuo, S.; Huang, J.; Tang, Z.; Xia, D. High-Entropy Modulated High-Spin Localized Cobalt Sites Enhance Catalytic Ozonation for Efficient Odor Control. *Angew. Chem., Int. Ed.* **2025**, *64* (29), No. e202507109.

(8) Qu, W.; Tang, Z.; Tang, S.; Wen, H.; Fang, J.; Lian, Q.; Shu, D.; He, C. Cation Substitution Induced d-Band Center Modulation on Cobalt-Based Spinel Oxides for Catalytic Ozonation. *Adv. Funct. Mater.* **2023**, *33* (44), 2301677.

(9) Zhang, J.-R.; Zhong, F.-Q.; Zhong, L.-B.; Dong, Z.-J.; Zhao, Q.-B.; Ao, Z.; Sun, D. D.; Yang, J.-C. E.; Zheng, Y.-M. Electron complementary effect of cerium tailored the electron/valence state of Mn-Ce dual-atom monolithic catalyst for enhanced Ozone catalysis. *Appl. Catal. B Environ.* **2025**, *373*, 125361.

(10) Tang, S.; Zhong, T.; Yao, Z.; Qu, W.; Li, T.; Zhao, H.; Tian, S.; He, C. Construction of Spatially Adjacent Ni and Co-Based Spinel Frustrated Lewis Pair Sites for Efficient Catalytic Ozonation. *Small* **2025**, *21* (21), 2500310.

(11) Sun, Y.; Liao, H.; Wang, J.; Chen, B.; Sun, S.; Ong, S. J. H.; Xi, S.; Diao, C.; Du, Y.; Wang, J.-O.; Breese, M. B. H.; Li, S.; Zhang, H.; Xu, Z. J. Covalency competition dominates the water oxidation structure-activity relationship on spinel oxides. *Nat. Catal.* **2020**, *3* (7), 554−563.

(12) Li, M.; Wang, X.; Liu, K.; Sun, H.; Sun, D.; Huang, K.; Tang, Y.; Xing, W.; Li, H.; Fu, G. Reinforcing Co−O Covalency via Ce(4f)−O(2p)−Co(3d) Gradient Orbital Coupling for High-Efficiency Oxygen Evolution. *Adv. Mater.* **2023**, *35* (30), 2302462.

(13) Zhou, Q.; Song, C.; Wang, P.; Zhao, Z.; Li, Y.; Zhan, S. Generating dual-active species by triple-atom sites through peroxymonosulfate activation for treating micropollutants in complex water. *Proc. Natl. Acad. Sci. U.S.A.* **2023**, *120* (13), No. e2300085120.

(14) Zou, J.; Lin, Y.; Yang, C. Covalency triggers high catalytic activity of amorphous molybdenum oxides for oxidative desulfurization. *Sci. China Chem.* **2023**, *66* (4), 1211−1220.

(15) Zhou, J.; Qiao, F.; Ren, Z.; Hou, X.; Chen, Z.; Dai, S.; Su, G.; Cao, Z.; Jiang, H.; Huang, M. Amorphization Engineering of Bimetallic Metal−Organic Frameworks to Identify Volcano-Type Trend toward Oxygen Evolution Reaction. *Adv. Funct. Mater.* **2024**, *34* (1), 2304380.

(16) Jia, B.; Liu, G.; Zhang, B.; Zheng, J.; Yin, K.; Lin, J.; Han, C.; Fan, X.; Xu, M.; Ye, L. General Modification Strategy on Amorphous Materials to Boost Catalytic Performance. *Adv. Funct. Mater.* **2024**, *34* (44), 2405867.

(17) Lu, W.; Yuan, M.; Chen, J.; Zhang, J.; Kong, L.; Feng, Z.; Ma, X.; Su, J.; Zhan, J. Synergistic Lewis acid-base sites of ultrathin porous Co_3O_4 nanosheets with enhanced peroxidase-like activity. *Nano Res.* **2021**, *14* (10), 3514−3522.

(18) Wei, Y.; Yi, L.; Wang, R.; Li, J.; Li, D.; Li, T.; Sun, W.; Hu, W. A Unique Etching−Doping Route to Fe/Mo Co-Doped Ni Oxyhydroxide Catalyst for Enhanced Oxygen Evolution Reaction. *Small* **2023**, *19* (37), 2301267.

(19) Qi, Y.; Xiao, X.; Mei, Y.; Xiong, L.; Chen, L.; Lin, X.; Lin, Z.; Sun, S.; Han, B.; Yang, D.; Qin, Y.; Qiu, X. Modulation of Brønsted and Lewis Acid Centers for $Ni_xCo_{3-x}O_4$ Spinel Catalysts: Towards Efficient Catalytic Conversion of Lignin. *Adv. Funct. Mater.* **2022**, *32* (15), 2111615.

(20) Su, R.; Gao, Y.; Chen, L.; Chen, Y.; Li, N.; Liu, W.; Gao, B.; Li, Q. Utilizing the oxygen-atom trapping effect of Co_3O_4 with oxygen vacancies to promote chlorite activation for water decontamination. *Proc. Natl. Acad. Sci. U.S.A.* **2024**, *121* (11), No. e2319427121.

(21) Ning, M.; Zhang, F.; Wu, L.; Xing, X.; Wang, D.; Song, S.; Zhou, Q.; Yu, L.; Bao, J.; Chen, S.; Ren, Z. Boosting efficient alkaline fresh water and seawater electrolysis via electrochemical reconstruction. *Energy Environ. Sci.* **2022**, *15* (9), 3945−3957.

(22) Da, Y.; Tian, Z.; Jiang, R.; Chen, G.; Liu, Y.; Xiao, Y.; Zhang, J.; Xi, S.; Chen, W.; Han, X.; Hu, W. Single-Atom Pt Doping Induced p-Type to n-Type Transition in NiO Nanosheets toward Self-Gating Modulated Electrocatalytic Hydrogen Evolution Reaction. *ACS Nano* **2023**, *17* (18), 18539−18547.

(23) Long, Y.; Zhu, X.; Gao, C.; Si, W.; Li, J.; Peng, Y. Modulation of Co spin state at Co_3O_4 crystalline-amorphous interfaces for CO oxidation and N_2O decomposition. *Nat. Commun.* **2025**, *16* (1), 1048.

(24) Mao, X.; Chang, C.-W.; Li, Z.; Han, Z.; Gao, J.; Lyons, M.; Sterbinsky, G.; Guo, Y.; Zhang, B.; Wang, Y.; Wang, X.; Han, D.; Yang, Q.-H.; Feng, Z.; Weng, Z. Sustainedly High-Rate Electroreduction of CO_2 to Multi-Carbon Products on Nickel Oxygenate/Copper Interfacial Catalysts. *Adv. Energy Mater.* **2024**, *14* (25), 2400827.

(25) Song, L.; Zhang, H.; Nie, Z.; Tian, J.; Liu, Y.; Ma, C.; Liu, P.; Ren, Q.; Xiong, J.; Huang, H.; Yang, W.; Cao, D.; Fu, M.; Ye, D. Ni Doping Promotes C−H Bond Activation and Conversion of Key Intermediates for Total Oxidation of Methane over Co_3O_4 Catalysts. *ACS Catal.* **2023**, *13* (24), 15779−15793.

(26) Liu, Y.; Ying, Y.; Fei, L.; Liu, Y.; Hu, Q.; Zhang, G.; Pang, S. Y.; Lu, W.; Mak, C. L.; Luo, X.; Zhou, L.; Wei, M.; Huang, H. Valence Engineering via Selective Atomic Substitution on Tetrahedral Sites in Spinel Oxide for Highly Enhanced Oxygen Evolution Catalysis. *J. Am. Chem. Soc.* **2019**, *141* (20), 8136−8145.

(27) Zhang, F.; Zhang, Y.; Wang, J.; Wang, Q.; Xu, H.; Li, D.; Feng, J.; Duan, X. Thermal Effect Management via Entropy Variation Strategy to Improve the Catalyst Stability in Acetylene Hydrogenation. *Angew. Chem., Int. Ed.* **2024**, *63* (45), No. e202412637.

(28) Zhang, Q.; Zheng, Z.; Gao, R.; Xiao, X.; Jiao, M.; Wang, B.; Zhou, G.; Cheng, H.-M. Constructing Bipolar Dual-Active Sites through High-Entropy-Induced Electric Dipole Transition for Decoupling Oxygen Redox. *Adv. Mater.* **2024**, *36* (26), 2401018.

(29) Wang, C.; Wang, K.; Feng, Y.; Li, C.; Zhou, X.; Gan, L.; Feng, Y.; Zhou, H.; Zhang, B.; Qu, X.; Li, H.; Li, J.; Li, A.; Sun, Y.; Zhang, S.; Yang, G.; Guo, Y.; Yang, S.; Zhou, T.; Dong, F.; Zheng, K.; Wang, L.; Huang, J.; Zhang, Z.; Han, X. Co and Pt Dual-Single-Atoms with Oxygen-Coordinated Co−O−Pt Dimer Sites for Ultrahigh Photocatalytic Hydrogen Evolution Efficiency. *Adv. Mater.* **2021**, *33* (13), 2003327.

(30) Sun, F.; Wang, G.; Ding, Y.; Wang, C.; Yuan, B.; Lin, Y. NiFe-Based Metal−Organic Framework Nanosheets Directly Supported on Nickel Foam Acting as Robust Electrodes for Electrochemical Oxygen Evolution Reaction. *Adv. Energy Mater.* **2018**, *8* (21), 1800584.

(31) Qiao, L.; Liu, D.; Zhu, A.; Feng, J.; Zhou, P.; Liu, C.; Ng, K. W.; Pan, H. Nickel-facilitated in-situ surface reconstruction on spinel Co_3O_4 for enhanced electrochemical nitrate reduction to ammonia. *Appl. Catal. B Environ.* **2024**, *340*, 123219.

(32) Zhang, H.; Zhou, H.; Wang, H.; Wang, Y.; Yang, X.; Wu, D.; Yuan, P.; He, M.; Wei, W.; Yang, T. Multihybridization for Enhancing

https://doi.org/10.1021/acs.est.5c11499
Environ. Sci. Technol. 2025, 59, 26292−26302

Fe−Ni Bimetal Electrocatalyst in Water Oxidation. *Adv. Energy Mater.* **2025**, *15* (13), 2403464.
(33) Wei, C.; Sun, Y.; Scherer, G. G.; Fisher, A. C.; Sherburne, M.; Ager, J. W.; Xu, Z. J. Surface Composition Dependent Ligand Effect in Tuning the Activity of Nickel−Copper Bimetallic Electrocatalysts toward Hydrogen Evolution in Alkaline. *J. Am. Chem. Soc.* **2020**, *142* (17), 7765−7775.
(34) Song, Q.; Li, J.; Wang, S.; Liu, J.; Liu, X.; Pang, L.; Li, H.; Liu, H. Enhanced Electrocatalytic Performance through Body Enrichment of Co-Based Bimetallic Nanoparticles In Situ Embedded Porous N-Doped Carbon Spheres. *Small* **2019**, *15* (44), 1903395.
(35) Nørskov, J. K.; Bligaard, T.; Logadottir, A.; Bahn, S.; Hansen, L. B.; Bollinger, M.; Bengaard, H.; Hammer, B.; Sljivancanin, Z.; Mavrikakis, M.; Xu, Y.; Dahl, S.; Jacobsen, C. J. H. Universality in Heterogeneous Catalysis. *J. Catal.* **2002**, *209* (2), 275−278.
(36) Hammer, B.; Nørskov, J. K. Electronic factors determining the reactivity of metal surfaces. *Surf. Sci.* **1995**, *343* (3), 211−220.

https://doi.org/10.1021/acs.est.5c11499
Environ. Sci. Technol. 2025, 59, 26292−26302